Mon. Not. R. Astron. Soc. **371,** 67–80 (2006) doi:10.1111/j.1365-2966.2006.10654.x

The OB binary HD 152219: a detached, double-lined, eclipsing system⋆

H. Sana,[1,2]† E. Gosset[1]‡ and G. Rauw[1]‡

[1]*Institut d'Astrophysique et de Géophysique, University of Liège, Allée du 6 Août 17, Bât. B5c, B-4000 Liège, Belgium*
[2]*European Southern Observatory, Alonso de Cordova 3107, Casilla 19001, Vitacura, Santiago 19, Chile*

Accepted 2006 June 1. Received 2006 May 30; in original form 2005 July 1

ABSTRACT

We present the results of an optical spectroscopic campaign on the massive binary HD 152219 located near the core of the NGC 6231 cluster. Though the primary to secondary optical brightness ratio is probably about 10, we clearly detect the secondary spectral signature and we derive the first reliable SB2 orbital solution for the system. The orbital period is close to 4.2403 d and the orbit is slightly eccentric ($e = 0.08 \pm 0.01$). The system is most probably formed by an O9.5 giant and a B1-2 V-III star. We derive minimal masses of 18.6 ± 0.3 and $7.3 \pm 0.1\,M_{\odot}$ for the primary and secondary, respectively, and we constrain the stellar radius at values about 11 and $5\,R_{\odot}$. *INTEGRAL*-Optical Monitoring Camera (OMC) data reveal that HD 152219 is the third O-type eclipsing binary known in NGC 6231. In the Hertzsprung–Russell (HR) diagram, the primary component lies on the blue edge of the β Cep-type instability strip and its spectral lines display clear profile variations that are reminiscent of those expected from non-radial pulsations. Finally, we report the analysis of *XMM–Newton* observations of the system. The X-ray spectrum is relatively soft and is well reproduced by a two-temperature mekal model with $kT_1 = 0.26$ keV and $kT_2 = 0.67$ keV. The X-ray flux is most probably variable on a time-scale of days. The average X-ray luminosity during our campaign is $\log(L_X) \approx 31.8$ (erg s^{-1}), but shows fluctuations of about 10 per cent around this value.

Key words: binaries: close – binaries: spectroscopic – stars: early-type – stars: individual: HD 152219 – X-rays: individual: HD 152219 – X-rays: stars.

1 INTRODUCTION

Though few in numbers, the O-type stars are among the brightest and most massive stellar objects found in galaxies. Although our comprehension is slowly increasing with the years, many issues are still lacking satisfactory answers. Among the more subtle aspects related to early-type stars, their intrinsic variability is still badly constrained. Clear-cut observational tests are difficult to establish and require a large amount of high-quality observations to properly map both the different time-scales of the phenomena and the different regions of the parameter space across the Hertzsprung–Russell (HR) diagram. An additional problem comes from the intrinsic difficulty to reliably derive the main physical parameters of these objects. In this regard, binaries have, since long ago, been considered as privileged laboratories. Indeed they potentially offer the possibility to measure stellar masses, radii and in some cases even distances.

We report here the results of our long-term optical high-resolution spectroscopic campaign on HD 152219. Located at 4.3 arcmin S-W from HD 152248, HD 152219 is one of the bright ($V = 7.56$) early-type binaries belonging to NGC 6231. Quoted spectral classifications range from O9.5 IV (Feinstein & Ferrer 1968) to B0.5 IV (Perry et al. 1990, hereafter PHYB90) whereas Levato & Malaroda (1980) reported O9.5 III. Projected rotational velocities were measured by Conti & Ebbets (1977) and Levato & Morrell (1983, hereafter LM83) who, respectively, derived values of 250 and 160 km s^{-1}. Three orbital solutions, quoting periods slightly larger than 4 d, have been published so far: Hill, Crawford & Barnes (1974, hereafter HCB74), LM83 and García & Mermilliod (2001, hereafter GM01). These will be described in Section 3.5. Quoting two papers in preparation, one by Perry et al. (most probably PHYB90) and another by Morris, Hill & Allison (which we could not find in the literature), HCB74 noted that 'this star is a light variable ($\Delta V \sim 0.10$ mag)'. Finally, focusing on the CCD photometry obtained these last 10 yr, we note that the published values for the V magnitude of HD 152219 are in the range 7.55 (Sung, Bessell & Lee 1998) to 7.66 (Balona & Laney 1995). This is similar to the above-mentioned work that quoted a 0.10-mag variation.

⋆Based on observations collected at the European Southern Observatory (La Silla, Chile) and with the *XMM–Newton* satellite, an ESA science mission with instruments and contributions directly funded by ESA Member States and the USA (NASA); also based on data from the Optical Monitoring Camera (OMC) Archive at LAEFF, processed by ISDC.

†E-mail: hsana@eso.org
‡FNRS Research Associate (Belgium).

Table 1. Journal of the spectroscopic observations of HD 152219. The first column gives the heliocentric JD (HJD −245 0000) at mid-exposure. The second column indicates the corresponding phase according to the He I ephemeris of Table 4. The next two columns provide the mean values of the RV measurements associated with the lines listed in Table 3. These were referred to a zero-systemic velocity frame before averaging. A 'n.' means that no reliable measurement could be performed for the secondary, either because of a lower signal-to-noise ratio or because of the important blend between the primary and secondary lines. The last column indicates the instrumental setting used.

HJD	$\phi_{\rm He\,I}$	$\overline{\rm RV_{1,\lambda}-\gamma_{1,\lambda}}$	$\overline{\rm RV_{2,\lambda}-\gamma_{2,\lambda}}$	Instr.
995.660	0.546	−118.6	n.	CAT
996.591	0.765	−3.6	n.	+ CES
997.608	0.005	92.3	n.	
998.595	0.238	14.8	n.	
999.603	0.476	−120.9	n.	
1000.572	0.704	−32.2	n.	
1299.808	0.836	13.3	n.	ESO 1.5-m
1300.802	0.071	−119.1	293.0	+ FEROS
1301.807	0.308	−3.2	n.	
1302.797	0.541	97.5	−248.6	
1304.806	0.015	−111.3	280.2	
1323.872	0.511	91.8	−232.6	
1327.805	0.439	62.5	−216.1	
1668.815	0.860	−18.5	n.	
1668.905	0.881	−38.6	n.	
1669.881	0.111	−113.4	272.4	
1670.872	0.345	14.1	n.	
1671.875	0.581	101.7	−254.9	
1672.800	0.800	20.8	n.	
1672.940	0.832	16.8	n.	
2037.824	0.883	−40.2	n.	
2037.914	0.905	−41.9	n.	
2039.811	0.352	14.7	n.	
2039.925	0.379	27.8	n.	
2040.806	0.587	105.9	−250.1	
2335.774	0.150	−95.7	256.8	
2335.814	0.159	−89.3	250.7	
2336.788	0.389	35.0	n.	
2337.765	0.619	100.7	−250.5	
2338.749	0.851	−3.3	n.	
2339.774	0.093	−117.4	286.4	
2381.671	0.973	−95.0	243.1	
2381.772	0.997	−104.8	267.2	
2382.668	0.209	−61.7	215.1	
2382.815	0.243	−36.0	n.	
2383.674	0.446	69.1	−207.7	
3130.655	0.607	98.7	−261.5	ESO 2.2-m
3130.856	0.655	96.0	−246.9	+ FEROS
3131.664	0.845	−0.6	n.	
3131.906	0.902	−40.6	n.	
3132.624	0.072	−122.5	295.6	
3132.897	0.136	−104.7	267.6	
3133.694	0.324	10.3	n.	
3133.902	0.373	29.0	n.	
3134.636	0.546	103.1	−258.4	
3134.890	0.606	102.7	−259.0	
3135.641	0.783	25.5	n.	
3135.882	0.840	7.8	n.	

The present paper is organized as follows. The observational material is described in Section 2. Section 3 presents the determination of the orbital properties of the system and compares our solution with earlier results. The evolutionary status and the physical parameters of the HD 152219 components are discussed in Section 4 and, in Section 5, we address the line profile variations in the primary spectrum. Section 6 presents the analysis of our X-ray observing campaign. Finally, Section 7 provides a summary of the main results of this work.

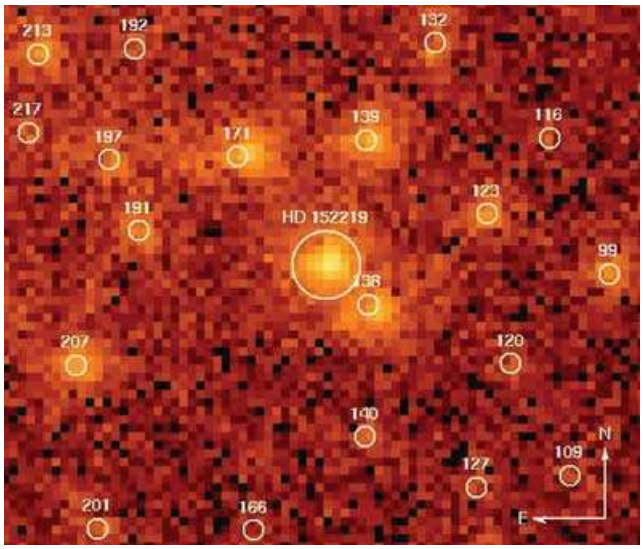

Figure 1. Cumulated (i.e. based on the merging of the six individual exposures) EPIC MOS1 + MOS2 image in the vicinity of HD 152219. The adopted source region is shown. Neighbouring X-ray sources are labelled using the internal numbering scheme of Sana et al. (2006a).

2 OBSERVATIONS AND DATA REDUCTION

2.1 Optical spectroscopy

The present work is based on 48 high-resolution spectra of HD 152219 obtained at the European Southern Observatory (ESO, La Silla, Chile). These were acquired during 35 different nights distributed over eight runs between 1998 July and 2004 May. The journal of the observations is presented in Table 1.

In 1998 July, six spectra in the range 4460–4480 Å (He I λ4471) were obtained at the ESO 1.4-m Coudé Auxiliary Telescope (CAT), with the Coudé Echelle Spectrograph (CES) equipped with the Very Long Camera. The detector used was ESO CCD#38, a Loral 2688×512 pixel CCD with a pixel size of 15 × 15 μm^2. The slit width was chosen to achieve a nominal resolving power of 70 000–80 000. The effective resolving power as derived from the full width at half-maximum (FWHM) of the lines of the ThAr calibration exposures was rather 65 000–75 000. Typical exposure times were 40 min and the average signal-to-noise ratio was about 100.

Between 1999 April and 2002 May, we collected 30 echelle spectra covering the whole optical range (∼3750–9200 Å) using the Fiber-Fed Extended Range Optical Spectrograph (FEROS), an echelle spectrograph mounted at the ESO 1.5-m telescope at La Silla. In 2004 May, 12 other FEROS spectra were obtained at the ESO 2.2-m telescope at La Silla. The detector was a 2 × 4 k^2 EEV CCD with a pixel size of 15 × 15 μm^2. The spectral resolving power of FEROS is 48 000. Typical exposure times ranged at the ESO 1.5-m telescope from 10 to 20 min according to the weather conditions, resulting in typical signal-to-noise ratios between 150 and 200. At the ESO 2.2-m telescope, thanks to increased instrument performances and to good weather conditions, the signal-to-noise ratio was above 250 for an exposure time of 15 min.

Table 2. Journal of the *XMM–Newton* observations of HD 152219. The mean JD is given in column 2. Columns 3–5 list the effective exposure times for the EPIC MOS1, MOS2 and pn instruments while columns 6–8 report the background-corrected count rates in the various instruments, as obtained using a 10-arcsec extraction region (see text). No correction for the EEF was applied. The last column provides the HD 152219 orbital phase for each *XMM–Newton* observation at mid-exposure. These were computed according to the He I-line ephemeris given in Table 4. The phase extension of a pointing is about 0.08. Obs. 2 and 4 however suffered from high background events that reduced the useful exposure time by about one third.

Obs. #	Mean JD	Effective duration (ks)			Count rates (10^{-3} count s^{-1})			$\phi_{\rm He\,I}$
	JD −245 0000	MOS1	MOS2	pn	MOS1	MOS2	pn	
1	2158.214	33.1	33.2	30.6	5.04 ± 0.40	6.01 ± 0.43	16.63 ± 0.75	0.275
2	2158.931	19.8	19.8	16.5	4.16 ± 0.45	4.34 ± 0.46	13.98 ± 0.86	0.444
3	2159.796	33.7	33.9	30.1	5.23 ± 0.40	5.35 ± 0.41	15.82 ± 0.72	0.648
4	2160.925	26.0	24.3	11.7	3.89 ± 0.37	3.12 ± 0.33	6.15 ± 0.47	0.915
5	2161.774	30.9	31.0	28.4	4.92 ± 0.41	6.05 ± 0.45	16.79 ± 0.78	0.115
6	2162.726	32.9	32.8	30.3	4.75 ± 0.39	5.58 ± 0.42	16.15 ± 0.74	0.339

The CES data were reduced in a standard way using the MIDAS package supported by ESO. The spectra were rectified by means of an instrumental response curve built from the observations, obtained under similar conditions, of a metal-poor 'reference' star (HD 203608: F6V). Finally, the spectra were normalized by fitting a low-order polynomial to the continuum. FEROS data were reduced using an improved version of the FEROS context (see details in Sana et al. 2003) working under the MIDAS environment. We mainly used the normalized individual orders. However, in case of doubts, we checked our results with the automatically merged spectrum.

2.2 X-ray observations

In 2001 September, the NGC 6231 open cluster was the target of an X-ray observing campaign with the *XMM–Newton* European Observatory (Jansen et al. 2001). The campaign, with a total duration of about 180 ks, is described in Sana et al. (2006a) together with the data reduction and source identification. We only give here a brief overview, focusing on the additional elements specific to HD 152219. Fig. 1 shows a view of the *XMM–Newton* field of view (FOV) in the vicinity of HD 152219. Table 2 provides the journal of the X-ray observations.

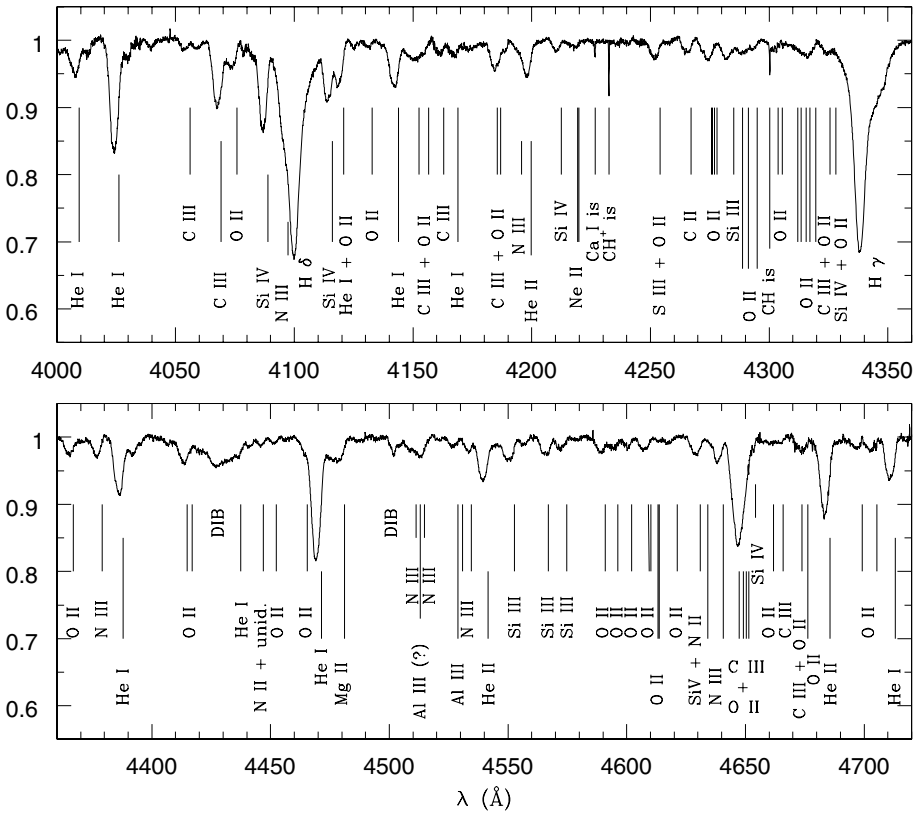

Figure 2. Blue spectrum of HD 152219 as obtained on HJD = 245 3132.624 ($\phi_{\rm He\,I} = 0.072$). The identification of the main lines has been indicated. The He I lines display a clear SB2 signature, with the blue-shifted primary and the red-shifted secondary components. The identification ticks refer to the rest wavelengths.

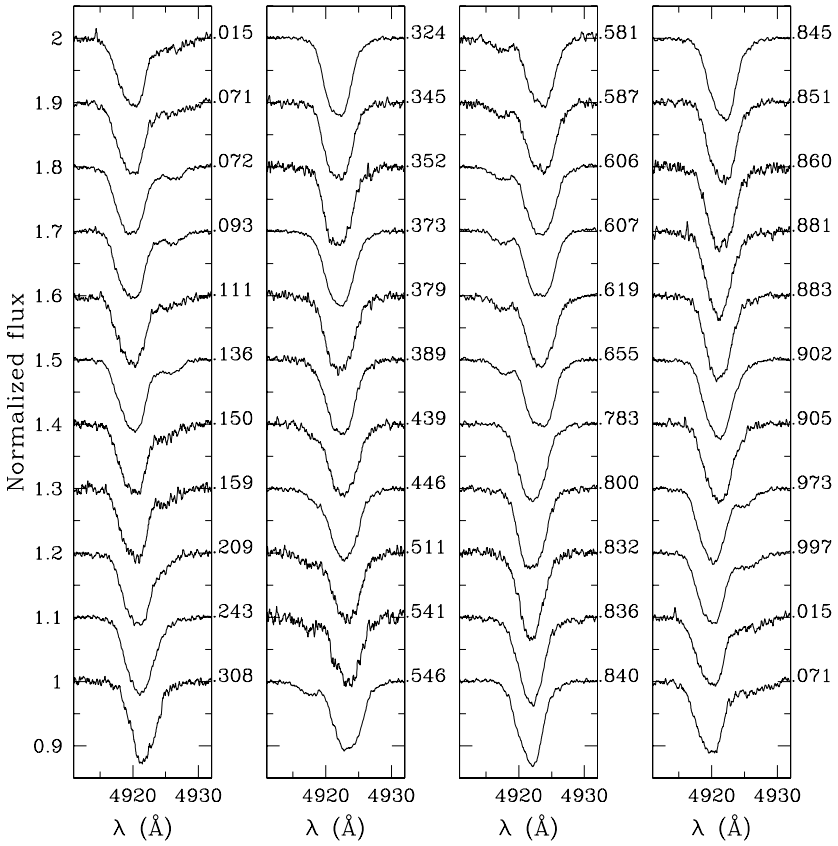

Figure 3. Variations, as observed in our FEROS spectra, of the He I λ4922 line as a function of the phase. Corresponding phases are indicated at right hand from each panel. The secondary spectral signature is clearly identified on the spectra obtained near quadratures ($\phi \sim 0.1$ and 0.6). Note also the variable primary line profile.

In the pn instrument, HD 152219 falls at less than 13 arcsec from a gap and the X-ray catalogue of the field (Sana et al. 2006a), which relies on a point spread function (PSF) fitting method, only considered the European Photon Imaging Camera (EPIC) MOS data. Using the Science Analysis System (SAS) task EVSELECT, we can however securely extract pn count rates in a circular region with a radius up to 10 arcsec. Because of the presence of an X-ray source at about 17 arcsec S-W of HD 152219 (X#138 according to the X-ray numbering defined in Sana et al. 2006a), the extraction of the X-ray light curves and spectra of HD 152219 was first limited to a radius of 8.5 arcsec. Because HD 152219 is brighter than X#138, we expect its signal to dominate in a radius of at least 10 arcsec. We performed the same analysis with this new radius value, but no difference was found in the results. We thus adopted the largest extraction region. According to the SAS task CALVIEW, a 10-arcsec radius at the position of HD 152219 corresponds to a PSF encircled energy fraction (EEF) of about 54 per cent. The extraction region was centred on the source position for all six pointings and for the three EPIC instruments. The different backgrounds were estimated from the very few source-free regions. The adopted source region is shown in Fig. 1. The corresponding background regions are presented in Sana et al. (2006b) together with a description of their positions and sizes.

Adopting these source and background regions, we extracted the HD 152219 count rates in different energy bands (see Section 6). Similarly, we extracted the source spectra in all EPIC instruments and for the six pointings individually. Unfortunately, the MOS1 instrument shows discrepant channels for Obs. 4, which draws the MOS1 count rate for this pointing towards higher values. The corresponding data set has thus been discarded in the analysis. Finally, we also extracted the merged spectrum in each instrument, thus combining the six observations of HD 152219. For this, we built the corresponding Ancillary Response Files (the so-called *arf* files) using the SAS task ARFGEN. We adopted the Redistribution Matrix Files (*rmf*) provided by the SOC and, for the pn, adapted to the particular position of HD 152219 on the detectors. The analysis of the X-ray data is presented in Section 6.

3 HD 152219 ORBITAL SOLUTION

3.1 The optical spectrum

The optical spectrum of HD 152219 (Fig. 2) is clearly dominated by the H I Balmer, He I and He II absorption lines. The metallic lines (C, N, O, Si and Mg ions) usually seen in O-type spectra can also be identified. All the He I lines and, to a lesser extent, the Balmer lines present a clear SB2 signature. However, because of the broad primary lines and of the large primary to secondary line intensity ratio, the two components are only disentangled at large separation (Fig. 3). The primary lines display variable profiles which, from time to time, broaden and flatten. The C III λ5696 line presents mixed absorption and emission that, at first sight, compensate each other. It also presents a variable profile. No other emission lines are seen in the spectrum of HD 152219.

We measured the line positions and equivalent widths (EWs) of a series of selected lines (Table 3) by adjusting Gaussian curves to the observed profiles. Depending on the separation of the double

Table 3. Orbital solutions deduced from different RV data sets. Each set corresponds to a particular spectral line (column 1). The upper part of the table corresponds to SB2 data sets while the lower part deals with SB1 primary measurements. The latter solutions also use the spectra obtained near conjunction phases and are thus based on a larger number of spectra than the corresponding SB2 solutions. The usual notations for the orbital elements have been used. s_y/s_x is the adopted ratio of the uncertainties associated with the secondary and primary RVs, respectively. As the period, the ratio s_y/s_x is part of the minimization process. Quoted uncertainties are the 1σ error bars.

Line	P (d)	s_y/s_x	e	ω (°)	K_1 (km s^{-1})	K_2 (km s^{-1})	γ_1 (km s^{-1})	γ_2 (km s^{-1})	rms (km s^{-1})
He I λ4026	4.24036	3.4	0.068 ± 0.015	157 ± 8	110.3 ± 0.7	283.2 ± 1.7	−23.2 ± 1.5	−7.6 ± 3.6	4.2
He I λ4388	4.24027	4.3	0.069 ± 0.015	156 ± 7	101.4 ± 0.9	269.9 ± 2.5	−12.7 ± 1.6	−19.6 ± 3.4	5.0
He I λ4922	4.24043	2.7	0.087 ± 0.009	160 ± 4	109.2 ± 0.4	282.0 ± 1.1	−15.3 ± 1.0	−33.1 ± 2.3	3.0
He I λ5876	4.24019	3.9	0.090 ± 0.015	152 ± 4	116.7 ± 0.8	288.5 ± 2.0	−22.7 ± 1.6	−21.1 ± 3.4	4.4
He I λ7065	4.24035	4.0	0.071 ± 0.012	149 ± 9	118.7 ± 1.0	276.2 ± 1.6	−18.8 ± 1.6	−17.3 ± 3.0	5.1
He I λ4026	4.24029	–	0.102 ± 0.016	139 ± 9	108.4 ± 1.8	–	−22.7 ± 1.2	–	7.5
Si IV λ4089	4.24029	–	0.110 ± 0.015	138 ± 8	126.6 ± 1.9	–	−20.1 ± 1.3	–	8.1
He I λ4388	4.24030	–	0.078 ± 0.020	146 ± 14	98.5 ± 1.9	–	−13.3 ± 1.3	–	8.3
He I λ4471	4.24026	–	0.082 ± 0.014	152 ± 11	110.4 ± 1.7	–	−31.8 ± 1.1	–	7.8
He II λ4541	4.24033	–	0.127 ± 0.020	137 ± 9	127.9 ± 2.6	–	−11.8 ± 1.7	–	10.8
He II λ4686	4.24032	–	0.123 ± 0.017	135 ± 7	128.2 ± 2.1	–	−16.9 ± 1.4	–	8.9
He I λ4922	4.24035	–	0.093 ± 0.014	146 ± 8	107.3 ± 1.5	–	−16.1 ± 1.0	–	6.3
O III λ5592	4.24034	–	0.142 ± 0.016	140 ± 6	124.7 ± 2.0	–	−17.4 ± 1.3	–	8.4
He I λ5876	4.24027	–	0.115 ± 0.012	140 ± 6	116.6 ± 1.5	–	−21.7 ± 1.0	–	6.2
He I λ7065	4.24027	–	0.099 ± 0.014	140 ± 8	117.5 ± 1.6	–	−19.5 ± 1.1	–	6.9

(SB2) lines, one or two Gaussians were simultaneously adjusted. Because of the presence of numerous metallic lines, some interesting lines are usually blended with neighbouring ones. In those cases where the line profiles are effectively affected by the surrounding lines, we carried out simultaneous multi-Gaussian fits. To compute the radial velocities (RVs) associated with the measured Doppler shifts, we mostly adopted the effective wavelengths for O-stars from Conti, Leep & Lorre (1977) below 4800 Å and from Underhill (1994) above. For the metallic lines that are not listed in these latter works, we used the rest wavelengths from Moore (1959). Measured RVs are listed in Appendix A.

3.2 Period determination

In the search for the orbital period P of the system, we applied both the method of Lafler & Kinman (1965) and the Fourier analysis of Heck, Manfroid & Mersch (1985, hereafter HMM; see also Gosset et al. 2001 for comments). The period search algorithms were applied on the RV data sets associated with most of the lines listed in Table 3. Because only the primary motion can reliably be followed throughout the orbit, we focused on the primary RVs. We systematically obtained period values in the range 4.24022–4.24048 d with an average of about 4.2403 d. As a test case, we also used the RV sets formed by the difference between primary and secondary velocities for a few SB2 lines. These sets are about twice less numerous but yielded similar results.

It is well known that the natural width of the peak in the periodogram is related to the extent of the time base T of the observations. A conservative approach to estimate the period uncertainty is to adopt a σ_P value that corresponds to one tenth of the peak width. This yields values of $\sigma_P = 8 \times 10^{-4}$ and 10^{-3} d, respectively, for the He I λ4471 RV set and for the other sets listed in Table 3. However, this does not account for the quality of the data nor for their actual distribution within the observing time base. A more refined approach, taking into account the emergence of the signal from the noise and certainly relevant for slightly eccentric orbits, was proposed by Lucy & Sweeney (1971). It yields values of σ_P in the range 5–8 $\times$ 10^{-5} d. The latter values are in agreement with the observed dispersion of the periods obtained from the orbital solution determinations corresponding to the various data sets (see Section 3.4).

3.3 The SB2 orbital solution

We first computed orbital solutions using the RV sets associated with the different absorption lines listed in Table 3. For SB1 lines, we used the algorithm of Wolfe, Horak & Storer (1967) in its original form and assigned the same weight to each measurement. For the sets associated with SB2 lines, we used a modified version of the algorithm. As explained in Rauw et al. (2000), we first adjusted the linear RV_2 versus RV_1 relation (which is independent of the adopted period value) using an orthogonal regression technique. The slope of this relation directly provides the mass ratio of the system. As in Sana et al. (2003), we then used the fitted parameters to transform the primary and secondary RVs into equivalent velocities of a fake SB1 system, of which the orbital elements are directly related to those of the physical SB2 system. In particular, it has the same period and eccentricity, and a semi-amplitude of the RV curve given by $\mathcal{K} = (K_1 K_2)^{1/2}$. The orbital elements of this equivalent system are then determined using the Wolfe et al. (1967) method and, as a last step, we deduced the true SB2 parameters from the obtained equivalent SB1 solution. In this approach, we have only considered those data points for which the RVs of the two components could be measured. In our derived solutions, we adopted a period value and a relative secondary to primary uncertainty ratio (s_y/s_x) that yield the lowest χ^2. Table 3 gives the best-fitting results and the corresponding root-mean-square (rms) residuals.

Finally, we also computed the mean RVs, on one hand, of the SB2 He I lines and, on the other hand, of all the primary lines quoted in Table 3. For this purpose, we shifted the individual RVs to a common frame before averaging them, taking into account the individual systemic velocities. The two orbital solutions obtained using the averaged primary and the He I RV measurements are given in Table 4

Table 4. Orbital and physical parameters of HD 152219 as deduced from different data sets: our averaged RVs computed over selected primary (SB1) lines (column 2), He I SB2 lines (column 3) and the SB1 data set extended by primary RVs reported in the literature (see Section 3.5). The usual notations have been used. T_0 is the time of periastron passage and is adopted as phase zero (i.e. $\phi = 0.0$). Note that the primary and the He I line solutions were computed in the zero-systemic velocity frame.

	Prim.	He I lines	Lit.
P (d)	4.24030	4.24032	4.240281
s_y/s_x	n.	3.3	n.
m_1/m_2	n.	2.530 ± 0.023	n.
e	0.108 ± 0.012	0.082 ± 0.011	0.095 ± 0.014
ω (°)	141 ± 6	153 ± 5	136 ± 8
T_0 (HJD	3200.026	3200.165	3199.960
−245 0000)	±0.073	±0.090	±0.002
K_1 (km s^{-1})	116.5 ± 1.4	110.7 ± 0.7	115.0 ± 1.5
K_2 (km s^{-1})	n.	279.9 ± 1.7	n.
γ_1 (km s^{-1})	−0.1±0.9	0.1 ± 1.2	−21.7±1.0
γ_2 (km s^{-1})	n.	−0.7±2.6	n.
$a_1 \sin i$ ($R_\odot$)	9.70 ± 0.12	9.24 ± 0.06	9.58 ± 0.13
$a_2 \sin i$ ($R_\odot$)	n.	23.36 ± 0.14	n.
$m_1 \sin^3 i$ ($M_\odot$)	n.	18.56 ± 0.27	n.
$m_2 \sin^3 i$ ($M_\odot$)	n.	7.34 ± 0.09	n.
rms (km s^{-1})	6.0	4.0	9.2

together with the physical parameters of the system. Fig. 4 displays the RV curves corresponding to the averaged He I SB2 solution.

3.4 HD 152219 orbital parameters

The best period values deduced from the different data sets of Table 3 are in excellent agreement; their average is $P = 4.24030 \pm 3 \times 10^{-5}$ and $4.24032 \pm 9 \times 10^{-5}$ d according either to the primary (SB1) or to the SB2 He I-line solutions. These mean values are further identical to the best-fitting values derived for the averaged solutions of Table 4. In the following, we adopt the latter SB2 solution as our final solution. We also adopt the apparent systemic velocities $\overline{\gamma_1} = -17.9$ km s^{-1} and $\overline{\gamma_2} = -22.3$ km s^{-1} for the primary and secondary components. These values were obtained as the weighted means of the systemic velocities associated with the two components in the various He I-line solutions of Table 3.

The common orbital parameters (P, e, ω) deduced in Table 3 show a good agreement, though a slight systematic shift between the SB1 and SB2 solutions can be observed. The latter solutions indeed tend to display a slightly lower eccentricity and a larger longitude of the periastron argument. From Table 4, the final SB1 and SB2 parameters are however in more acceptable agreement. Part of the observed differences might result from the fact that the SB2 solutions were computed using only those points for which the two components are disentangled. These are thus located near quadrature only. From Fig. 4, it is clear that the primary points show larger deviations from the best-fitting RV curve near conjunction phases. Accounting for those points or not might thus lead to slightly different results.

Finally, we note that different lines yield significantly different values for the semi-amplitudes of the RV curves (K) and for the apparent systemic velocities (γ). While different values of γ are commonly found in early-type binaries and are considered to result from the formation of the different lines in different regions of the expanding atmosphere, the discrepancies in K are less common. These are however directly seen in the RV measurements of

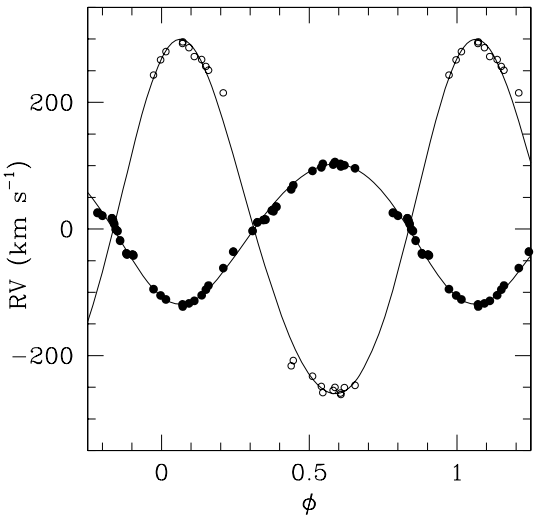

Figure 4. HD 152219 RV curves corresponding to the He I solution of Table 4 plotted in the zero-systemic velocity frame. The FEROS RV measurements listed in Table 1 have been overplotted. Filled and open symbols are for the primary and secondary components, respectively.

HD 152219 and do not result from a bias in the fitting method. A putative interpretation is that the front and rear sides of the star do not provide similar line formation conditions, a phenomenon which can affect the various lines in a different way.

3.5 A combined orbital solution

As mentioned in the Introduction, three SB1 orbital solutions have previously been published: HCB74, LM83 and GM01. HCB74 obtained 16 RV measurements over 8 d and, including three other measurements later quoted by PHYB90, proposed a first SB1 orbital solution: $P = 4.16 \pm 0.04$ d, $e = 0.10 \pm 0.06$ and $K = 117.4 \pm 3.8$ km s^{-1}. With four additional RV points, and using the HCB74 data, LM83 derived a similar orbital solution with a period $P = 4.16572 \pm 7 \times 10^{-6}$ d, and a slightly larger eccentricity $e = 0.14 \pm 0.04$. Using the same data sets and the same period values as HCB74 and LM83, we recomputed their orbital solutions and found them in good agreement with the published values. We could however not reproduce the PHYB90 point at RV ~ 40 km s^{-1} as seen in the RV curve of HCB74 (their fig. 3). We suspect that the observed discrepancy comes from an erroneous Julian Date (JD) quoted by PHYB90 and we excluded the corresponding point from the RV curve adjustments. The orbital period derived from our CES and FEROS data sets $P \sim 4.24$ d is slightly but significantly different from the period found by these authors. Again adopting their respective RV sets, we used the period search algorithms mentioned in Section 3.2. We found a large number of almost indiscernible aliases corresponding to periods between 4.09 and 4.27 d (nine aliases) for HCB74 and between 4.09 and 4.37 d (>40 aliases) for LM83. Clearly the orbital periods derived by these authors were ill constrained.

More recently, GM01 obtained eight additional spectra of the object and announced to have detected the spectral signature of the companion in three of them. Adopting a slightly shorter period $P = 4.069597 \pm 3.4 \times 10^{-5}$ d, they derived an SB2 orbital solution characterized by a much larger eccentricity $e = 0.22 \pm 0.06$. They presented three profiles of the Hγ line obtained at three different phases (their fig. 4). Though the primary RV shift is clearly seen, the secondary spectral signature is quite unclear. In addition, according

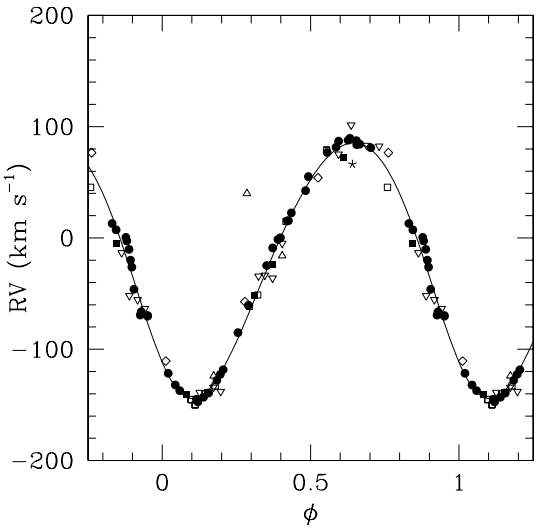

Figure 5. HD 152219 primary RV curve computed using both the literature data and the mean of the primary SB1 measurements (the latter were corrected for the systemic velocity obtained from the various lines before averaging). The weighted mean systemic velocity $\overline{\gamma_1} = -19.9\,\mathrm{km\,s^{-1}}$ (obtained from the SB1 solutions listed in Table 3) has then been adopted to combine the actual data with the previous observations. Different symbols indicate different data sets. Open symbols are from previous work observations: PHYB90, upward triangles; HCB74, downward triangles; Conti et al. (1977), asterisk; LM83, diamonds; corrected GM01 data, squares. Filled symbols indicate new RV points from the present work: CES, squares; FEROS, circles. Note that the PHYB90 point at RV = 40 km s^{-1}, near $\phi \approx 0.35$, was rejected for period search and orbital solution determination.

to their RV curves (their fig. 1a), the observed primary motion does clearly not correspond to the quoted phases. As we already discussed in Sana et al. (2003), these authors reported confusing JD which corrupted their period search and their orbital solution determination. We further note that, compared to our high-quality data, GM01 have underestimated the secondary absolute RVs, and thus the amplitude of the secondary RV curve. We will thus not consider their orbital solution further, but we will account for their primary RV measurements after correction for the quoted JD (Mermilliod, private communication).

Finally, we combined all the literature RV measurements with the data from the present work. This yields a total of 79 observations[1] covering a time-span of 13 186 d. We performed a new period search and obtained $P \approx 4.24028$ d. The associated uncertainty, corresponding to one tenth of the periodogram peak natural width, amounts to 1.4×10^{-4} d while the one provided by the Lucy & Sweeney (1971) formula is of the order of 10^{-6} d. However, the hypothesis of equipartition of the measurements over the time-span is strongly at odds in the latter case. Using the Wolfe et al. (1967) algorithm, we computed a joined orbital solution. The best-fitting parameters are displayed in Table 4 and the corresponding RV curve is shown in Fig. 5. This latter solution is in very good agreement with the other solutions quoted in Table 4, giving further support to our adopted solution. The time of conjunction indicated by the He I-line solution corresponds to phases $\phi = 0.30$ (primary in front) and $\phi = 0.85$ (secondary in front).

[1]These 79 observations include the corrected data from GM01. The discrepant point at 40 km s^{-1} from PHYB90 has however been rejected.

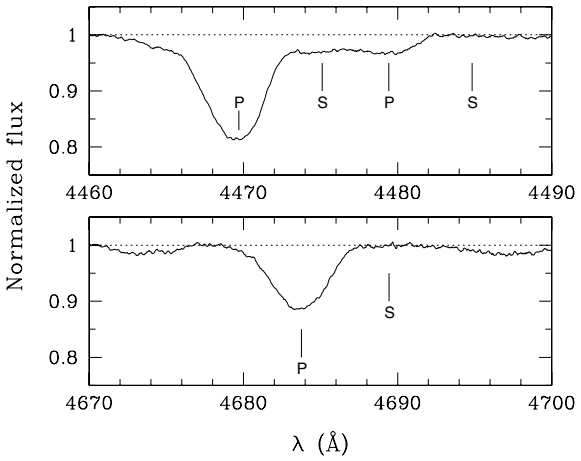

Figure 6. He I λ4471/Mg II λ4481 and He II λ4686 regions in the HD 152219 spectrum obtained at HJD ≈ 245 3132.897 ($\phi_{\mathrm{He\,I}} = 0.136$). The tick marks indicate the expected positions of the primary (P) and secondary (S) lines.

4 HD 152219 PHYSICAL PARAMETERS

4.1 Spectral types and luminosity classes

4.1.1 Primary component

The spectral signature of the primary component is clearly dominant in the spectrum of HD 152219. We adopted the classification criteria from Conti (1973b) as adapted to late O-stars by Mathys (1988). They are based on the EW ratio of the He I λ4471 and He II λ4542 lines. Doing this, we only considered the EWs measured on the spectra where the two components are disentangled. We obtained a mean $\log W' (W_{\lambda4471}/W_{\lambda4542}) = 0.48 \pm 0.04$ which corresponds to a spectral type O9.5, with spectral type O9 within 1σ.

To determine the luminosity class, we adopted the criterion from Conti & Alschuler (1971) based on the EW ratio of the Si IV λ4089 and He I λ4144 lines. We obtained $\log W''(W_{\lambda4089}/W_{\lambda4144}) = 0.17 \pm 0.04$, which leads to a giant luminosity class. We also measured $\log W''' = \log(W_{\lambda4388}) + \log(W_{\lambda4686}) = 5.31 \pm 0.03$. According to Mathys (1988), this rules out a supergiant class. This also indicates a giant classification, unless $l_1 = (L_1/L_{\mathrm{tot}}) < 0.81$. The optical brightness of both components will be discussed in Section 4.2.

4.1.2 Secondary component

The main spectral signatures of the secondary star are the Balmer and He I lines. For the latter, we have been able to measure the positions and EWs with a good confidence. At our detection level, we clearly note the absence of the He II λλ4542, 4686 and Mg II λ4481 lines at the positions predicted by the orbital solution (Fig. 6). The lack of He II lines definitively excludes an O spectral type and, at our detection threshold, most probably indicates a spectral subtype later than B0.5 (Walborn & Fitzpatrick 1990). To refine our subtype classification, we carefully searched for the presence of secondary metallic lines in our FEROS spectra. We could not rule out the existence of faint Si IV and Si III lines. If these latter are present, their EWs are probably below 0.02 Å. In the metallic lines, the secondary spectral signature could only be clearly disentangled in the S III+O II λ4254 complex and in the C II λ4267 line on our highest signal-to-noise ratio FEROS spectra. These two lines have an EW about 0.01 and 0.02 Å, respectively. Clearly neither the signal-to-noise ratio nor the spectral resolution of the instrument is the limiting

factors here. We rather emphasize the broadness of the lines and the probably large intensity ratio between the primary and secondary lines. Because at our detection level, we do not clearly detect the C III+O II complex at λλ4650-60, we suppose that the secondary is a main-sequence star (however see below). Similarly, we adopt a spectral type B1-B2 which, according to Walborn & Fitzpatrick (1990), corresponds to the minimum of the Mg II λ4481 line. Indeed, we would expect to detect the He II λ4686 line if the star were hotter, and the Mg II λ4481 line if it were cooler.

4.2 Optical brightness ratio and evolutionary status

We roughly estimated the optical brightness ratio based on the dilution of the primary and secondary lines in the spectrum of HD 152219. For this purpose, we compared the mean EWs of the primary lines with typical (averaged) EWs of O9.5 stars (Conti & Alschuler 1971; Conti 1973a; Mathys 1988). Based on the He I λλ4026, 4144, 4388, 4471, He II λλ4542, 4686 and Si IV λ4089 lines, we obtained an average brightness ratio of $l_1 = 0.86 \pm 0.05$ and 0.99 ± 0.05 assuming, respectively, a main sequence or a giant class. We also compared the secondary line strengths to the typical EWs reported by Didelon (1982). We focused on the He I λλ4026, 4144 and 4388 lines. We obtained $l_2 = (L_2/L_{\rm tot})$ in the range 0.07–0.10 considering B1-2 V-III stars. We adopt the average value $l_2 \approx 0.09 \pm 0.01$. According to Didelon (1982), this value is in agreement with most of the metallic lines being too diluted for being observed in the HD 152219 spectrum. Let us recall that we rejected the giant classification for the secondary on the basis of the C III+O II complex at λλ4650-60 not being observed. With such a value for l_2, it would only be marginally detectable for a giant B1-2 star. The luminosity class of the secondary is thus still uncertain from the sole spectroscopy.

In the following discussion, we adopt a primary to secondary brightness ratio corresponding to $l_1 = 0.91 \pm 0.05$, thus opting for a conservative value of the uncertainty. Sung (private communication) reported $V = 7.560$ and $B - V = 0.165$ for the system. Using $R = 3.3$ (Sung et al. 1998), adopting the absolute colours quoted by Schmidt-Kaler (1982) and a distance modulus DM = 11.07 ± 0.04 (Sana et al. 2006a, and references therein), preliminary computations indicate that the system probably harbours a giant primary star, in agreement with the spectroscopic classification. To estimate the confidence interval of the following results, we considered, for the primary star, the neighbouring subspectral type O9 and B0 III. For the secondary, we adopted the central values corresponding to a B1.5 star, and to B0.5 and B2.5 stars as confidence limits. We obtained $M_{\rm V} = -5.03 \pm 0.09$, yielding $M_{\rm V,1} = -4.93 \pm 0.11$ and $M_{\rm V,2} = -2.42 \pm 0.69$. According to Humphreys & McElroy (1984), these values are typical for giant and main-sequence stars of the quoted spectral type. For the secondary, this includes the giant class at 1σ. Using the bolometric corrections from Humphreys & McElroy (1984), we obtained $M_{\rm bol,1} = -7.93 \pm 0.13$ and $M_{\rm bol,2} = -4.62 \pm 0.77$, unless the secondary is actually a giant, in which case we have $M_{\rm bol,2} = -4.22 \pm 0.83$.

Finally, the Humphreys & McElroy (1984) effective temperature scale indicates $T_{\rm eff}^{\rm O9.5\,III} = 31.9^{32.8}_{30.3}$ kK and $T_{\rm eff}^{\rm B1.5\,V} = 21.8^{25.9}_{19.2}$ kK (resp. $T_{\rm eff}^{\rm B1.5\,III} = 20.0^{25.9}_{17.6}$ kK). We thus obtained primary and secondary stellar radii of $R_1 = 11.2 \pm 1.1\,{\rm R}_\odot$ and $R_2 = 5.2 \pm 2.7\,{\rm R}_\odot$ (resp. $5.2 \pm 3.6\,{\rm R}_\odot$). These values are again in excellent agreement with typical O9.5 III and B1-2 V parameters. Because of the large errors associated with the secondary, we cannot rule out a B1-2 giant nature. Comparing with the evolutionary tracks and isochrones from Schaller et al. (1992), we estimated the primary evolutionary age to be about 5 Myr, which is in agreement with the cluster age as determined from previous photometric studies (PHYB90; Balona & Laney 1995; Raboud, Cramer & Bernasconi 1997; Baume, Vázquez & Feinstein 1999). From a rough interpolation of the evolutionary tracks, the primary had an initial mass about $24\,{\rm M}_\odot$, corresponding to an actual mass close to $23.3\,{\rm M}_\odot$, thus slightly lower than typical O9.5 III masses ($26\,{\rm M}_\odot$ according to Howarth & Prinja 1989).

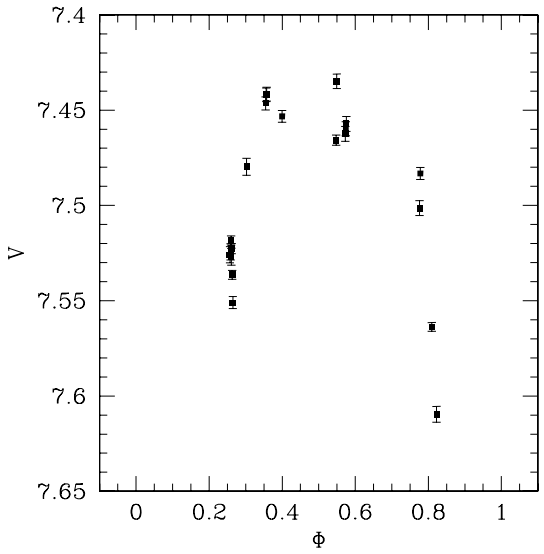

Figure 7. OMC light curve of HD 152219 folded through our ephemerides. Only data points with a zero offset from the centre of the 5 × 5 pixel box are plotted.

We made an estimate of the projected rotational velocity $V \sin i$ of the primary component through a comparison of the measured FWHMs of the various lines quoted in Table 3 with those measured, for a range of $V \sin i$, on model spectra of equivalent effective temperature and gravity (see the above discussion). The latter spectra were computed using the codes TLUSTY and SYNSPEC (Lanz & Hubeny 2003, and references therein) that use line blanketed, non-local thermodynamic equilibrium, plane-parallel, hydrostatic atmospheres. The He I lines yield consistent results with a mean value about $190\,{\rm km\,s^{-1}}$, suggesting that the primary star has not reached quasi-synchronous rotation yet (which would correspond to a projected rotational velocity close to $140\,{\rm km\,s^{-1}}$). However, the O III λ5592 and Si IV λ4089 lines indicate significantly smaller values of 175 and $150\,{\rm km\,s^{-1}}$, respectively, while the He II λ4686 and λ4542 lines point towards $V \sin i$ values of 160 and $130\,{\rm km\,s^{-1}}$. The estimated 1σ error on these measurement is below $10\,{\rm km\,s^{-1}}$. Finally, we used the formula of Eggleton (1983) to estimate the Roche lobe radii. Adopting $i \approx 63^\circ$ (see Section 4.3), we found that the primary and secondary components are filling about 30 and 10 per cent of their Roche lobe volume, respectively. Both stars are thus well within their Roche lobe limits.

4.3 An eclipsing binary

From Table 4, we note that the minimal masses are quite large, suggesting a large orbital inclination. Comparing the values of Table 4 with typical O9.5 III masses, we obtain an inclination i of 63°. The secondary mass should then correspond to $10.3\,{\rm M}_\odot$, thus agreeing with the adopted spectral type. Using the constraints deduced on the component radii, we find that the limiting inclination above which eclipses may occur in the system lies around 62°. Clearly, HD 152219 is a limiting case.

To check whether the system displays photometric eclipses, we have retrieved the *V*-band photometry of the star from the *INTEGRAL*-Optical Monitoring Camera (OMC) Archive at LAEFF (Gutiérrez et al. 2004). 129 photometric data points of HD 152219 were obtained (Swings, private communication). When folded with our ephemerides, these data clearly indicate drops in the optical emission (∼0.1–0.18 mag) at phases close to the expected times of conjunction according to our RV curves. However, the raw OMC light curve also displays a large dispersion (∼0.05 mag) at phases outside the expected times of the photometric eclipses. Actually, the OMC photometry is extracted over a 5×5 pixel^2 window (one pixel corresponding to 17.5×17.5 arcsec^2) around the source. In a crowded field such as NGC 6231, neighbouring sources can introduce a highly structured background thereby considerably reducing the photometric accuracy (Gutiérrez et al. 2004). We have therefore restricted ourselves to the data obtained with a zero offset between the source and the extraction box. In this way, the dispersion is considerably reduced, but at the expense of a significant reduction of the number of data points (21 points remaining). The resulting light curve is shown in Fig. 7. The two eclipses are clearly seen though the data are certainly not of a sufficient quality to perform a more quantitative analysis of the light curve. The larger deviations of the primary data points from the best-fitting RV curve near the primary conjunction (Fig. 4) can now be interpreted as an eclipse effect (the so-called Rossiter–McLaughlin effect).

5 LINE PROFILE VARIABILITY (LPV) OF THE PRIMARY

As illustrated in Fig. 3, the primary lines display variable profiles with, from time to time, a flattened core and/or asymmetric wings. Similar profile variations appear in all the primary lines. In particular, they are also seen in the Si IV λ4089, Mg II λ4481, He II λ4686, O III λ5592 and C IV λ5812 lines. The latter ones do not show the secondary signature and the variations can therefore not be attributed to the sole blending of the primary and secondary line profiles.

In a first approach of the phenomenon, we have focused on the He II λ4686 line, which is probably the most suitable line for our purpose: it is reasonably strong, well isolated and unaffected by the secondary spectral signature. The line profiles might display heavy changes in two spectra obtained the same night (see e.g. the two spectra obtained the last night of our campaign at $\phi = 0.783$ and 0.840). Our observing strategy is thus clearly not optimized to study time-scales that short. The tightest follow up was performed in 2004 May when HD 152219 was observed twice a night for six consecutive nights. As a first step, we thus focus exclusively on the He II λ4686 profiles acquired in 2004 May. We used both the time variance spectrum (TVS) analysis of Fullerton, Gies & Bolton (1996) and a two-dimensional (2D) Fourier analysis (Rauw et al. 2001). In this latter method, the HMM Fourier analysis is performed at each wavelength step. It thus provides a 2D Fourier chart that allows to identify the different frequencies at work in different parts of the studied profile. Prior to the analysis, the He II λ4686 line has been brought to the primary star velocity frame using the primary orbital solution of Table 4 and the He II λ4686 apparent systemic velocity of -16.7 km s^{-1} (Table 3). For comparison, we applied a similar analysis on a line-free wavelength range (λλ4738-4748 Å) located in the same FEROS echelle order as the He II λ4686 line. Fig. 8 displays the average He II λ4686 profile over the 2004 May run and the results of the TVS analysis. It confirms that the line presents very significant variations. The 2D Fourier chart suggests

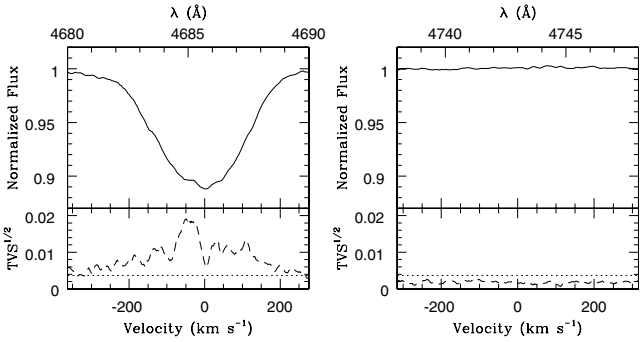

Figure 8. Mean spectrum (plain lines) and square root of the TVS (dashed lines) of the He II λ4686 line profile (left) and of a reference continuum domain (right). The dotted lines give the 0.01 significance level. Both the wavelength and RV scales are indicated. The velocities are expressed in the reference frame of the primary.

that different frequencies are probably at work in different parts of the lines.

Although the other observing periods provide a less appropriate coverage and display a lower signal-to-noise ratio on average, we also applied a similar analysis. The amplitude of the TVS is much more limited compared to their respective 0.01 significance levels. Briefly, they indicate that the He II λ4686 line is variable during the different runs, though the location of the most prominent variabilities in the line profile could be quite different from that observed in 2004. We note that the observed differences could be due to an uneven sampling of the underlying phenomenon during the different observing runs. Finally, we also note that the He II λ5412 line displays similar results to those of the He II λ4686 line. However, the line is partly affected by a neighbouring blend. Results associated with the O III λ5592 line are less conclusive, probably because of the lower signal-to-noise ratio for this line. Clearly, extending the present study to other lines in the primary spectrum may help to clarify the nature of the variations. This will however require to *clean* the HD 152219 spectrum from the secondary signature.

The possible reasons for the observed profile variations in the primary spectrum are numerous. Among the most probable, we can mention an underlying emission component, corotating wind structures (e.g. Rauw et al. 2001), magnetic confinement (ud-Doula & Owocki 2002) and non-radial pulsations. Although our current time series is too scarce to provide clear-cut observational constraints, indirect considerations might yield a first insight into the nature of the LPV. In early-type stars, the Balmer and He lines can harbour an emission component that might influence their observed profile. HD 152219 is however not a particularly hot O-type star and the emission is expected to remain very faint. In addition, the metallic lines should not be affected. Therefore, an underlying emission component is probably not the cause for the observed modulations. The fact that no trace of wind emission is found in the Balmer lines further indicates that the wind of the primary is not particularly strong, which is clearly not in favour of any wind-related effect. Then, one can note that the location of the HD 152219 primary component in the HR diagram corresponds to the blue edge of the β Cep-type pulsational instability strip computed by Kiriakidis, Fricke & Glatzel (1993, see also Pamyatnykh 1999). Fullerton et al. (1996) performed a survey of the line profile variations of a sample of O-type stars and found a good correlation with these predictions. Finally, the observed line profile variations and the subsequent TVS profiles are reminiscent of those produced by NRPs (e.g. Fullerton et al. 1996). There are at least two other known O9.5 stars that display NRPs

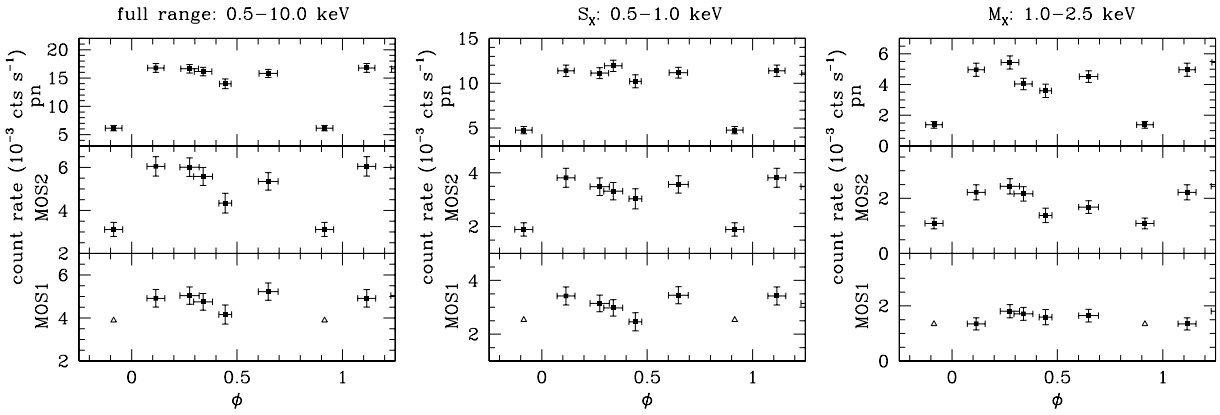

Figure 9. Broad-band X-ray light curves in the three EPIC instruments. The different energy ranges considered are indicated on top of each panel. The vertical bars give the 1σ uncertainty on the background-corrected count rates. The horizontal bars indicate the duration of each pointing. The open triangles provide the measured count rates for the discrepant MOS1 observation (see text).

(ζ Oph, Kambe et al. 1997; HD 93521, Howarth & Reid 1993), although both of them are main-sequence stars. Interestingly enough, their main frequencies correspond to periods of a couple of hours. Our current time series is however too sparse to address such rapid variations. Therefore, although the main frequency candidates obtained for the core of the He IIλ4686 line are indeed beyond one cycle per day, these results should be considered as very preliminary.

6 X-RAY OBSERVATIONS

As mentioned in Section 2.2, we adopted, for the three EPIC instruments and for the six pointings, a final extraction region of 10-arcsec radius centred on the source position. We derived the count rates in the total energy band (0.5–10.0 keV) and in three smaller energy ranges: a soft (S_X) band (0.5–1.0 keV), an intermediate (M_X) band (1.0–2.5 keV) and a hard (H_X) band (2.5–10.0 keV). The hard band only accounts for a few photons and the obtained count rates show large uncertainties. We thus focused on the other energy ranges. The broad-band light curves, displayed in Fig. 9, present similar shapes but with a quite different amplitude between the MOS1 and MOS2. However, this mainly results from the fact that the Obs. 4 count rate near $\phi = 0.9$ is probably overestimated because of some apparently discrepant channels (see Section 2.2), a still unsolved problem which unfortunately happens at the time of the most significant variability indicated by the two other instruments. Indeed, both the MOS2 and the pn light curves show a clear pointing-to-pointing variation. A χ^2 test performed on the MOS2 and pn count rates rejects the null hypothesis of constant count rates throughout the six pointings at the 0.01 significance level in the various energy bands quoted in Fig. 9, thus leaving little doubt on the variability of the observed X-ray emission from HD 152219.

In the next step, we extracted the HD 152219 X-ray spectra for each pointing and for each instrument, using the same source and background extraction regions as previously adopted for the light curves. The obtained X-ray spectra are relatively soft and peak around 0.8–0.9 keV. To characterize the properties of the emitting plasma, we adjusted optically thin thermal plasma MEKAL models (Mewe, Gronenschild & van den Oord 1985; Kaastra 1992). The MOS and pn spectra were adjusted simultaneously using the XSPEC software v.11.2.0 (Arnaud 1996). We adopted an equivalent interstellar column of neutral hydrogen of $N_{\rm H,ISM} = 0.27 \times 10^{22}\,{\rm cm}^{-2}$. A single temperature model was insufficient to adequately describe the observed spectra, except for Obs. 2. We thus adopted a two-temperature (2-T) model allowing for possible local absorption for both MEKAL components. Preliminary results indicate that the absorption column associated with the lower temperature component tends to be systematically close to zero. Lower residuals and more stable solutions are obtained by removing this parameter from the fit. Best-fitting results are quoted in Table 5. Only a slight variation can be seen in the parameters, the HD 152219 X-ray spectrum being somewhat softer when the emissivity is lower. Finally, for each of the EPIC instrument, we extracted the combined spectrum from the merging of the six X-ray observations. We also used a 2-T MEKAL model to fit the obtained spectra and the best parameters are given in the last line of Table 5. The spectra and the best-fitting models are plotted in Fig. 10. From the Berghöfer et al. (1997) relations and adopting either a luminosity class V or III, the expected intrinsic emission from the two stellar components amounts to about log $(L_X) \approx 31.8$ (erg s^{-1}) (in the 0.2–2.0 keV band). Though the energy ranges considered here are not exactly identical, the observed luminosities from the system are in very good agreement with this value (see Table 6). Similarly, the expression for the canonical relation in the 0.5–10.0 keV energy range recently derived from the analysis of the X-ray properties of all the O-type stars in NGC 6231 (Sana et al. 2006b) also predicts an X-ray luminosity log $(L_X) \approx 31.8$ (erg s^{-1}). In this sense, the HD 152219 system cannot be considered as significantly X-ray overluminous.

Although the X-ray light curve does not have an optimal phase coverage, we propose now a possible interpretation of the observed modulations. Interestingly enough, the minimum of the emission level is reached close to the time of the primary conjunction (at $\phi \approx 0.85$) and one could, at first sight, think of an occultation effect. However, it is well known that the emitting volume in early-type stars typically extends over several stellar radii. Hence, the secondary component will hardly occult a significant fraction of the primary X-ray emission. This rather suggests the presence of an additional emission component localized in between the two stars. In this regard, an extra emission resulting from a wind interaction is one of the most natural ways to produce such a localized component.

Using the constraints on the physical parameters deduced in the previous section, we estimated the wind parameters for the HD 152219 components following the mass-loss recipes of Vink, de Koter & Lamers (2000, 2001). In doing so, we assumed an orbital inclination of 63°. As expected, the primary wind is overwhelmingly dominant and no ram pressure equilibrium is possible along the system axis. This suggests that the primary wind may crash into

Table 5. Results of the simultaneous fits of the three EPIC spectra with XSPEC. The model used was $\mathrm{wabs_{ISM}}$ * ($\mathrm{mekal_1}$ + $\mathrm{wabs_2}$ * $\mathrm{mekal_2}$). The term $\mathrm{wabs_{ISM}}$ was fixed to the interstellar value ($N_{\mathrm{H,ISM}} = 0.27 \times 10^{22}$ cm^{-2}). The first and second columns give the phase and the observation number. The next five columns (columns 3–7) provide the best-fitting parameters while column 8 lists the corresponding reduced χ^2 and the associated number of degrees of freedom (d.o.f.). N_{H} yields the absorbing column (in units 10^{-22} cm^{-2}). kT is the model temperature (in keV) while norm is the norm factor [expressed in 10^{-5} cm^{-5}, norm $= (10^{-14}/4\pi d^2) \int n_{\mathrm{e}} n_{\mathrm{H}}\, dV$ with d, the distance to the source (in cm), n_{e} and n_{H}, the electron and hydrogen number densities (in cm^{-3})]. The quoted upper and lower values provide the limits of the 90 per cent confidence interval. Columns 9–12 provide the observed fluxes (in 10^{-14} erg cm^{-2} s^{-1}) in the 0.5–10.0 keV energy band and in the $\mathrm{S_X}$ (0.5–1.0 keV), $\mathrm{M_X}$ (1.0–2.5 keV) and $\mathrm{H_X}$ (2.5–10.0 keV) bands, respectively.

ϕ [1]	Obs. # [2]	kT_1 [3]	$\mathrm{norm_1}$ [4]	$N_{\mathrm{H},2}$ [5]	kT_2 [6]	$\mathrm{norm_2}$ [7]	χ^2_ν (d.o.f.) [8]	f_{X} [9]	$f_{\mathrm{X,S}}$ [10]	$f_{\mathrm{X,M}}$ [11]	$f_{\mathrm{X,H}}$ [12]
0.275	1	$0.26^{0.29}_{0.21}$	$8.3^{9.9}_{6.7}$	$0.36^{0.56}_{0.20}$	$0.70^{0.77}_{0.57}$	$6.5^{8.9}_{5.1}$	0.82 (74)	7.3	4.3	2.8	0.2
0.444	2	$0.24^{0.34}_{0.15}$	$6.0^{8.7}_{2.9}$	$0.12^{0.45}_{0.00}$	$0.61^{0.77}_{0.50}$	$5.2^{8.7}_{2.4}$	0.78 (38)	6.7	4.3	2.3	0.1
0.648	3	$0.30^{0.33}_{0.19}$	$7.8^{9.5}_{4.9}$	$0.41^{1.01}_{0.01}$	$0.71^{0.78}_{0.56}$	$4.4^{7.6}_{3.2}$	1.06 (72)	6.8	4.3	2.4	0.1
0.915[a]	4	$0.19^{0.39}_{0.08}$	$5.0^{27.1}_{1.4}$	$0.00^{3.18}_{0.00}$	$0.58^{n.}_{0.46}$	$4.2^{6.3}_{1.1}$	1.08 (21)	5.9	3.9	1.9	0.1
0.115	5	$0.22^{0.27}_{0.18}$	$8.0^{11.1}_{5.9}$	$0.00^{0.34}_{0.00}$	$0.69^{0.79}_{0.61}$	$4.8^{6.5}_{3.5}$	1.31 (69)	6.9	4.4	2.4	0.1
0.339	6	$0.28^{0.34}_{0.20}$	$6.3^{8.2}_{3.9}$	$0.25^{0.64}_{0.03}$	$0.62^{0.74}_{0.55}$	$5.5^{7.8}_{3.2}$	0.94 (67)	6.7	4.1	2.4	0.1
Merged	–	$0.26^{0.29}_{0.22}$	$7.5^{8.2}_{6.5}$	$0.22^{0.35}_{0.11}$	$0.67^{0.72}_{0.63}$	$5.0^{5.4}_{4.2}$	1.09 (268)	6.9	4.3	2.4	0.1

[a]The simultaneous fit was restrained to the MOS2+pn instruments (see text).

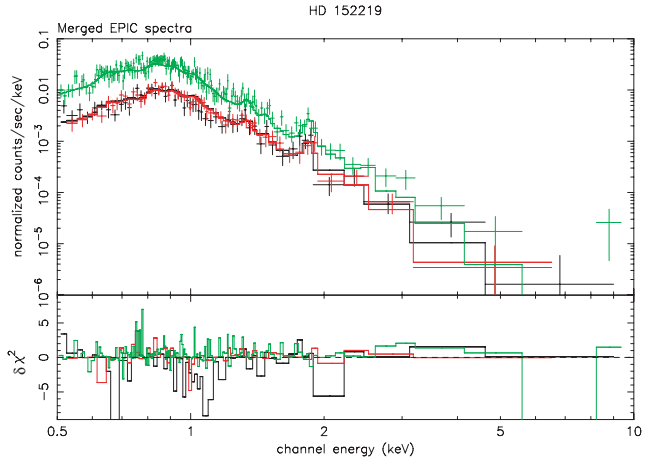

Figure 10. Combined X-ray spectra of HD 152219. Different colours indicate different instruments: MOS1, black; MOS2, red; pn, green. The best-fitting model of Table 5 is given by the plain lines. The bottom panel shows the contributions of individual bins to the χ^2 of the fit. The contributions are carried over with the sign of the deviation (in the sense data minus model). This figure appears in colour in the electronic edition of the journal.

the secondary star surface. The X-ray emission produced by such an interaction in a purely adiabatic case is about a few 10^{30} erg s^{-1} (Usov 1992), which is thus one order of magnitude smaller than the intrinsic contribution of the two stellar components. However, it is roughly of the same order of magnitude than the observed modulations in the HD 152219 X-ray luminosity (around 7–8 $\times$ 10^{30} erg s^{-1}). In such a model, the minimum of the X-ray emission arises when the secondary is presenting its rear side to the observer, around $\phi \sim 0.8$–0.9, thus occulting any emission produced on its inner side. We thus propose that HD 152219 displays a similar wind interaction as CPD $-$ 41°7742, an O9 V+B0.5 V massive binary in NGC 6231 (Sana et al. 2005). This suggests that such a phenomenon might be more widely spread than previously expected. Unfortunately, because of the longer period of HD 152219, our X-ray data do not provide a dense phase coverage and critical phases are missed. In addition, the HD 152219 eccentricity, though limited, induces a distance variation of at least 15 per cent between apastron and periastron, which will influence the strength of the primary wind at the distance of the secondary surface. Clearly, a better phase coverage of the HD 152219 system in the X-rays combined with additional modelling that accounts for the system orientation and for the eccentricity of the orbit are needed to provide better constraints on the observed variability.

Table 6. Unabsorbed fluxes ($f^{\mathrm{un.}}$, expressed in 10^{-14} erg cm^{-2} s^{-1}) corresponding to the best-fitting 2-T models of Table 5 and corrected using the adopted interstellar absorbing column $N_{\mathrm{H,ISM}} = 0.27 \times 10^{22}$ cm^{-2}. The last column gives the X-ray luminosity (in erg s^{-1}) in the 0.5–10.0 keV band, assuming DM = 11.07.

ϕ	Obs. #	$f^{\mathrm{un.}}_{\mathrm{X}}$	$f^{\mathrm{un.}}_{\mathrm{X,S}}$	$f^{\mathrm{un.}}_{\mathrm{X,M}}$	$f^{\mathrm{un.}}_{\mathrm{X,H}}$	$\log L_{\mathrm{X}}$
0.275	1	20.4	16.2	4.0	0.2	31.82
0.444	2	18.8	15.3	3.5	0.1	31.78
0.648	3	18.8	15.1	3.6	0.1	31.78
0.915	4	17.3	14.4	2.8	0.1	31.74
0.115	5	20.6	17.0	3.5	0.2	31.82
0.339	6	18.1	14.3	3.6	0.1	31.76
Merged	–	19.5	15.8	3.6	0.1	31.80

7 SUMMARY

We present the results of an optical spectroscopic monitoring campaign on the early-type binary HD 152219, located near the core of the NGC 6231 open cluster in the Sco OB 1 association. Although the absorption lines are broad in the HD 152219 spectrum, we report the clear detection of the secondary component. We find that previous period determinations suffered from strong aliasing or were corrupted. The orbital elements deduced from the analysis of different line Doppler shifts are in good agreement, except for the semi-amplitudes of the RV curves and for the systemic velocities. The latter two parameters indeed present significant differences from spectral line to spectral line that can also be seen in the different sets of RV measurements. Our final period value, $P \sim 4.2403$ d, further allows us to reproduce all the RV observations obtained since the late 1960s. We confirm that the system has a slight eccentricity $e = 0.08 \pm 0.01$ and we determine a primary to secondary mass

ratio of 2.53 ± 0.02. The two components have minimal masses of, respectively, 18.6 ± 0.3 and $7.3 \pm 0.1\,M_{\odot}$, while we estimated radii of 11 and $5\,R_{\odot}$, respectively.

Based on spectroscopic criteria, we find that HD 152219 is most probably formed by an O9.5 giant primary and a B1-2 V-III secondary. From the comparison of primary and secondary line EWs with typical line strengths of stars of similar spectral types, we estimate the brightness ratio to correspond to $l_1 = L_1/L_{\rm tot} = 0.91 \pm 0.05$, a value which is rather independent of the assumption on the luminosity classes. Finally, *INTEGRAL*-OMC observations reveal that HD 152219 is most probably an eclipsing binary, though the quality of the data is too limited to provide reliable constraints on the physical and orbital parameters of the system.

The primary component of HD 152219 shows clear line profile variations that similarly affect most of the lines in its spectrum. We note that HD 152219 is located on the blue edge of the β Cep-type pulsational instability strip in the HR diagram (Kiriakidis et al. 1993; Pamyatnykh 1999) and that the observed variations are reminiscent of those produced by non-radial pulsation modes (e.g. Fullerton et al. 1996). Clearly, dedicated observations combining high signal-to-noise ratio, high spectral resolution and a tight follow up of the possibly short time-scale variations should help to better constrain the nature of the phenomenon at work in this particularly interesting system.

Finally, we also reported the analysis of the *XMM–Newton* X-ray observations of HD 152219, which were acquired during a 5-d campaign towards the NGC 6231 cluster (Sana et al. 2006a). Broad-band X-ray light curves built from MOS2 and pn data indicate strong variability on a time-scale of days. The HD 152219 X-ray spectrum is relatively soft and peaks at energies about 0.8–0.9 keV. The averaged spectrum is well described by a 2-T MEKAL model with an unabsorbed lower temperature component ($kT_1 = 0.26$ keV) and a moderately absorbed slightly hotter component ($kT_2 = 0.67$ keV). The mean X-ray luminosity of the source, about $\log(L_{\rm X}) \approx 31.8$ (erg s^{-1}), is in good agreement with the amount of X-ray emission expected from the individual stellar contributions of the two components of the binary. It however presents fluctuations of about 10 per cent around this mean value. These fluctuations are further correlated with slight changes in the X-ray spectral parameters, the flux being slightly harder when the emission level is higher and slightly softer otherwise.

ACKNOWLEDGMENTS

We are grateful to J.-P. Swings for providing us with the OMC photometry of HD 152219. It is a pleasure to thank M. De Becker for assistance in handling the TVS and 2D Fourier analyses, as well as N. Linder who ran the TLUSTY and SYNSPEC codes. We also thank the referee, Dr I.D. Howarth, for his careful reading of the manuscript. The authors are greatly indebted towards the 'Fonds National de la Recherche Scientifique' (FNRS), Belgium, for multiple supports. Part of this work was also supported by the PRODEX XMM and Integral conventions, contracts P4/05 and P5/36 'Pôle d'Attraction Interuniversitaire' (Belgium).

REFERENCES

Arnaud K. A., 1996, in Jacoby G., Barnes J., eds, ASP Conf. Ser. Vol. 101, Astronomical Data Analysis Software and Systems (ADASS) V. Astron. Soc. Pac., San Francisco, p. 17
Balona L. A., Laney C. D., 1995, MNRAS, 276, 627
Baume G., Vázquez R. A., Feinstein A., 1999, A&AS, 137, 233
Berghöfer T. W., Schmitt J. H. M. M., Danner R., Cassinelli J. P., 1997, A&A, 322, 167
Conti P. S., 1973a, ApJ, 179, 161
Conti P. S., 1973b, ApJ, 179, 181
Conti P. S., Alschuler W. R., 1971, ApJ, 170, 325
Conti P. S., Ebbets D., 1977, ApJ, 213, 438
Conti P. S., Leep E. M., Lorre J. J., 1977, ApJ, 214, 759
Didelon P., 1982, A&AS, 50, 199
Eggleton P. P., 1983, ApJ, 268, 368
Feinstein A., Ferrer O. E., 1968, PASP, 80, 410
Fullerton A. W., Gies D. R., Bolton C. T., 1996, ApJS, 103, 475
García B., Mermilliod J. C., 2001, A&A, 368, 122 (GM01)
Gosset E., Royer P., Rauw G., Manfroid J., Vreux J.-M., 2001, MNRAS, 327, 435
Gutiérrez R., Solano E., Domingo A., García J., 2004, in Ochsenbein F., Allen M. G., Egret D., eds, ASP Conf. Ser. Vol. 314, Astronomical Data Analysis Software and Systems (ADASS) XIII. Astron. Soc. Pac., San Francisco, p. 153
Heck A., Manfroid J., Mersch G., 1985, A&AS, 59, 63 (HMM)
Hill G., Crawford D. L., Barnes J. V., 1974, AJ, 79, 1271 (HCB74)
Howarth I. D., Prinja R. K., 1989, ApJS, 69, 527
Howarth I. D., Reid A. H. N., 1993, A&A, 279, 148
Humphreys R. M., McElroy D. B., 1984, ApJ, 284, 565
Jansen F. et al., 2001, A&A, 365, L1
Kaastra J., 1992, An X-Ray Spectral Code for Optically Thin Plasmas. Internal SRON-Leiden Report, updated version 2.0
Kambe E. et al., 1997, ApJ, 481, 406
Kiriakidis M., Fricke K. J., Glatzel W., 1993, MNRAS, 264, 50
Lafler J., Kinman T. D., 1965, ApJS, 11, 216
Lanz T., Hubeny I., 2003, ApJS, 146, 417
Levato H., Malaroda S., 1980, PASP, 92, 323
Levato H., Morrell N., 1983, Astrophys. Lett., 23, 183 (LM83)
Lucy L. B., Sweeney M. A., 1971, AJ, 76, 544
Mathys G., 1988, A&AS, 76, 427
Mewe R., Gronenschild E. H. B. M., van den Oord G. H. J., 1985, A&AS, 62, 197
Moore C. E., 1959, A Multiplet Table of Astrophysical Interest. Part 1. NBS Technical Note, Rev. edn. US Department of Commerce, Washington
Pamyatnykh A. A., 1999, Acta Astron., 49, 119
Perry C. L., Hill G., Younger P. F., Barnes J. V., 1990, A&AS, 86, 415 (PHYB90)
Raboud D., Cramer N., Bernasconi P. A., 1997, A&A, 325, 167
Rauw G., Sana H., Gosset E., Vreux J.-M., Jehin E., Parmentier G., 2000, A&A, 360, 1003
Rauw G., Morrison N. D., Vreux J.-M., Gosset E., Mulliss C. L., 2001, A&A, 366, 585
Sana H., 2005, PhD thesis, Liège University, Belgium
Sana H., Hensberge H., Rauw G., Gosset E., 2003, A&A, 405, 1063
Sana H., Antokhina E., Royer P., Manfroid J., Gosset E., Rauw G., Vreux J.-M., 2005, A&A, 441, 213
Sana H., Gosset E., Rauw G., Sung H., Vreux J.-M., 2006a, A&A, 454, 1047
Sana H., Rauw G., Nazé Y., Gosset E., Vreux J.-M. 2006b, MNRAS, in press
Schaller G., Schaerer D., Meynet G., Maeder A., 1992, A&AS, 96, 269
Schmidt-Kaler T., 1982, in Schaifer K., Voigt H. H., eds, Landolt-Bornstein New Series, Vol. 2b, Astronomy and Astrophysics, Stars and Star Clusters. Springer-Verlag, Berlin
Sung H., Bessell M. S., Lee S., 1998, AJ, 115, 734
ud-Doula A., Owocki S. P., 2002, ApJ, 576, 413
Underhill A. B., 1994, ApJ, 420, 869
Usov V. V., 1992, ApJ, 389, 635
Vink J. S., de Koter A., Lamers H. J. G. L. M., 2000, A&A, 362, 295
Vink J. S., de Koter A., Lamers H. J. G. L. M., 2001, A&A, 369, 574
Walborn N. R., Fitzpatrick E. L., 1990, PASP, 102, 379
Wolfe R. H., Horak H. G., Storer N. W., 1967, in Hack M., ed., The Machine Computation of Spectroscopic Binary Elements. Modern Astrophysics, A Memorial to Otto Struve. Gordon & Breach Science Publishers, New York, p. 251

APPENDIX A: RV MEASUREMENTS

For the sake of completeness, we provide in Tables A1 and A2 the primary and secondary RVs measured on the various individual lines listed in Table 3. Sana (2005) has shown that a RV accuracy of about 1 km s^{-1} can be obtained for such measurements using good quality FEROS spectra of non-peculiar O-type stars. The case of HD 152219 is however more complicated because of the observed LPVs. Indeed the line profiles may deviate significantly from the adopted Gaussian model. While the fit probably still provides a good estimate of the line centroid, the direct estimate of the RV uncertainties from the Gaussian fit results is unreliable. We have thus adopted a simpler approach, giving a similar weight to each RV point for a given component (see Section 3.3 for more details). However, the uncertainties on the RV measurements are probably of the order of a few km s^{-1} as indicated a posteriori by the various orbital solution rms.

Table A1. Measured primary and secondary RVs on various SB2 lines of the HD 152219 spectrum. A 'n.' means that no reliable measurement could be performed for the secondary, either because of a lower signal-to-noise ratio or because of the important blend between the primary and secondary lines.

HJD	He I λ4026		He I λ4388		He I λ4922		He I λ5876		He I λ7065	
−245 0000	RV_1	RV_2	RV_1	RV_2	RV_1	RV_2	RV_1	RV_2	RV_1	RV_2
1299.808	−8.7	n.	−1.8	n.	−17.1	n.	0.6	n.	0.7	n.
1300.802	−140.8	283.7	−122.5	258.5	−134.3	267.5	−146.4	282.5	−144.1	274.2
1301.807	−29.1	n.	−15.0	n.	−19.1	n.	−23.1	n.	−22.4	n.
1302.797	75.4	−270.7	79.0	−264.9	83.6	−280.4	77.9	−259.7	84.9	n.
1304.806	−135.6	268.3	−113.7	255.1	−126.0	270.0	−138.5	260.8	−135.3	248.3
1323.872	73.8	−247.9	71.4	−238.6	76.0	−273.8	72.1	−251.3	77.0	n.
1327.805	28.8	n.	30.4	n.	41.8	n.	39.8	−237.2	44.6	n.
1668.815	−39.6	n.	−26.2	n.	−32.3	n.	−42.1	n.	−44.8	n.
1668.905	−57.2	n.	−39.9	n.	−52.0	n.	−67.5	n.	−69.1	n.
1669.881	−135.9	259.8	−114.2	246.0	−127.7	246.2	−141.9	291.4	−140.1	219.8
1670.872	−9.0	n.	−1.2	n.	−0.9	n.	−6.8	n.	−4.3	n.
1671.875	79.0	−261.7	83.2	−258.8	86.7	−291.8	84.1	−288.8	89.8	n.
1672.800	−2.3	n.	−2.9	n.	3.6	n.	7.4	n.	5.5	n.
1672.940	−2.5	n.	−3.8	n.	−2.1	n.	−0.9	n.	0.6	n.
2037.824	−58.4	n.	−42.9	n.	−53.6	n.	−69.4	n.	−69.6	n.
2037.914	−61.2	n.	−42.8	n.	−52.8	n.	−72.9	n.	−72.4	n.
2039.811	−9.5	n.	−1.0	n.	−3.4	n.	−3.4	n.	−1.8	n.
2039.925	1.7	n.	6.2	n.	12.0	n.	11.3	n.	15.3	n.
2040.806	84.2	−262.5	85.6	−256.4	88.4	−298.5	86.6	−278.8	92.1	−253.1
2335.774	−123.1	276.6	−101.9	213.2	−113.2	220.4	−124.7	−124.7	−121.1	−121.1
2335.814	−113.7	252.9	−101.6	220.1	−103.7	218.9	−119.3	−119.3	−118.9	−118.9
2336.788	8.9	n.	12.2	n.	20.1	n.	19.5	n.	21.5	n.
2337.765	79.4	−265.1	81.4	−268.7	82.0	−282.9	85.9	−266.5	77.2	n.
2338.749	−25.0	n.	−16.0	n.	−18.2	n.	−24.4	n.	−25.6	n.
2339.774	−139.1	285.6	−118.6	235.0	−132.2	260.5	−146.4	274.5	−143.4	277.7
2381.671	−115.1	236.2	−98.3	203.1	−110.1	207.3	−123.5	243.6	−120.8	226.8
2381.772	−125.3	261.2	−108.4	234.3	−119.2	232.6	−133.1	258.5	−130.8	250.7
2382.668	−77.7	n.	−67.9	204.5	−74.9	n.	−87.4	n.	−86.9	188.7
2382.815	−55.6	n.	−43.1	n.	−51.5	n.	−61.7	n.	−60.9	n.
2383.674	36.8	n.	50.9	−236.7	51.4	n.	51.8	−219.4	54.0	n.
3130.655	74.9	−280.1	77.6	−278.1	80.7	−288.9	80.4	−281.4	87.1	−277.7
3130.856	72.7	−267.3	72.1	−254.5	77.7	−274.7	78.5	−268.4	86.2	−268.2
3131.664	−20.4	n.	−12.4	n.	−15.3	n.	−19.6	n.	−28.0	n.
3131.906	−59.9	n.	−39.8	n.	−53.5	n.	−71.9	n.	−70.8	n.
3132.624	−145.0	286.6	−123.8	275.5	−136.6	263.0	−150.8	280.7	−149.0	273.6
3132.897	−126.0	260.6	−109.2	230.4	−118.8	247.5	−131.3	252.2	−130.7	248.7
3133.694	−12.9	n.	−4.9	n.	−4.9	n.	−9.6	n.	−9.0	n.
3133.902	2.5	n.	5.7	n.	10.0	n.	12.8	n.	21.1	n.
3134.636	79.5	−274.9	83.0	−267.5	83.7	−289.9	84.9	−277.5	91.5	−280.7
3134.890	76.4	−265.5	82.4	−274.0	83.5	−291.4	86.5	−280.9	92.2	−281.7
3135.641	1.6	n.	2.1	n.	7.7	n.	10.1	n.	13.1	n.
3135.882	−14.8	n.	−8.2	n.	−8.5	n.	−13.1	n.	−9.1	n.

Table A2. Measured primary RVs on various lines of the HD 152219 spectrum.

HJD −245 0000	Si IV λ4089 RV_1	He I λ4471 RV_1	He II λ4541 RV_1	He II λ4686 RV_1	O III λ5592 RV_1
995.660		150.4			
996.591		−35.4			
997.608		60.5			
998.595		−17.0			
999.603		−152.7			
1000.572		−64.0			
1299.808	4.5	−11.2	5.5	4.2	5.0
1300.802	−152.4	−153.8	−145.1	−151.8	−150.1
1301.807	−30.9	−33.5	−26.1	−24.1	−17.0
1302.797	85.6	66.9	91.7	91.5	87.0
1304.806	−145.8	−136.2	−143.1	−148.4	−141.3
1323.872	88.7	66.4	77.7	90.3	82.5
1327.805	54.3	29.7	53.3	51.2	59.1
1668.815	−46.6	−55.3	−62.1	−53.9	−50.4
1668.905	−81.4	−70.4	−87.9	−79.1	−80.2
1669.881	−148.1	−147.6	−140.3	−146.7	−142.8
1670.872	0.7	−13.5	22.0	2.5	5.2
1671.875	92.0	71.0	113.2	95.7	91.4
1672.800	14.4	−11.6	29.4	15.7	21.5
1672.940	5.7	−11.0	6.0	14.5	6.5
2037.824	−80.3	−72.6	−55.2	−75.3	−77.7
2037.914	−80.5	−79.6	−66.2	−79.6	−80.6
2039.811	2.8	−17.6	27.4	7.2	9.3
2039.925	22.2	−9.4	45.2	26.3	31.7
2040.806	94.4	72.7	112.2	99.5	86.3
2335.774	−130.2	−131.1	−120.2	−131.4	−120.5
2335.814	−124.4	−123.7	−121.3	−124.8	−124.4
2336.788	29.8	13.4	36.7	34.1	37.4
2337.765	94.5	71.8	98.3	94.6	85.7
2338.749	−32.9	−35.5	−23.9	−32.5	−19.9
2339.774	−153.9	−150.2	−142.7	−150.0	−146.3
2381.671	−130.0	−128.5	−126.7	−130.3	−126.9
2381.772	−139.2	−128.4	−143.4	−139.2	−145.8
2382.668	−93.7	−94.0	−84.3	−90.7	−85.8
2382.815	−69.9	−72.0	−57.4	−66.5	−58.7
2383.674	60.7	56.2	75.7	58.7	62.7
3130.655	92.4	66.4	98.3	99.0	89.5
3130.856	90.7	64.4	96.2	92.8	88.0
3131.664	−19.9	−35.4	−10.5	−12.1	−16.9
3131.906	−81.3	−77.5	−78.5	−78.8	−83.1
3132.624	−157.5	−156.5	−144.7	−149.5	−151.9
3132.897	−136.4	−129.2	−125.6	−133.4	−129.8
3133.694	−10.5	−20.9	−1.0	−2.4	−5.2
3133.902	21.9	−0.5	31.2	32.0	24.4
3134.636	92.6	72.9	99.8	99.2	90.3
3134.890	94.6	72.5	102.9	97.5	93.9
3135.641	17.6	−4.2	30.4	30.1	29.0
3135.882	−6.3	−27.5	−1.7	−1.1	−3.0

This paper has been typeset from a TEX/LATEX file prepared by the author.